Available online at www.sciencedirect.com
ScienceDirect
International Journal of Heat and Mass Transfer 51 (2008) 4216–4227
International Journal of HEAT and MASS TRANSFER
www.elsevier.com/locate/ijhmt

Application of the proper orthogonal decomposition to turbulent convective flows in a simulated Czochralski system

S. Rahal [a,*], P. Cerisier [b], H. Azuma [c]

[a] Department of Mechanical Engineering, University of Batna, Rue Boukhlouf Mohamed el Hadi, 05000 Batna, Algeria
[b] IUSTI – CNRS UMR 6595, Polytech'Marseille, Technopôle de Château-Gombert, 5 rue Enrico Fermi, 13453, Marseille, France
[c] Department of Aerospace Engineering, Osaka Prefecture University, Gakuen-cho 1-1, Sakai, Osaka 599-8531, Japan

Received 23 August 2007; received in revised form 26 December 2007
Available online 18 April 2008

Abstract

The aim of this work is to show the benefit of using various new methods in studying the general aspects of the convective flow in a simulated Czochralski system. We considered the influence of the crystal rotation (Reynolds number from 0 to 3.9×10^3) and buoyancy (Rayleigh number from 0 to 7.2×10^7). Velocity fields, obtained by an ultrasonic technique, the corresponding 2D Fourier spectra and a correlation function have been used. Steady, quasi-periodic and turbulent states, were recognized. The complex space–time dynamics of the flow were reduced to a binary code of the velocity fields. Thanks to the binary representation, the transition to turbulence in the Czochralski flow was found to occur via spatiotemporal intermittency. The orthogonal decomposition method was applied and the numbers of modes, involved in the dynamics of turbulent flows, calculated. As expected, the increase of the buoyancy effects induces more modes to be involved in the dynamics. The increase of the rotation effects reduces the number of modes and oscillations. The reconstruction coefficients, obtained using the proper orthogonal decomposition method, were found to reflect accurately the actual flow. The various analysis methods used in this paper allowed reaching complementary results and corroborating conclusions.

Keywords: Czochralski; Convection; Ultrasound; Turbulence; Orthogonal decomposition

1. Introduction

Although several methods have been used to manufacture silicon crystals, the so-called Czochralski (Cz) crystal puller method is widely used for industrial production. This fact comes from the ability of the Cz method to meet the stringent requirements for purity and crystallographic perfection. A comprehensive introduction and review of the research carried out on this flow, prior to 1997, can be found in [1]. More recently, other papers dealing with the Cz convective system have been published [2–6]. These papers were mainly devoted to the numerical modelling of the flow instabilities and the application of a magnetic field to suppress the flow oscillations.

The melt flow in a Czochralski crucible during silicon crystal growth influences the quality of the grown crystals [7]. Indeed, the melt flow oscillations are known to have an especially strong influence upon microdefects and striations which appear in the final crystal and which are detrimental to the quality of semi-conductor devices made from it [8]. Thus, a more complete understanding of the fluid flow in silicon melts is essential.

Recently, much effort has been devoted to producing large-sized crystals to increase the productivity of semiconductor industry [8]. Since the size of the Czochralski crucible has to be large, the assumption of a laminar flow may not be generally valid. Indeed, the large values of Reynolds (Re) and Rayleigh (Ra) numbers for such extended systems imply that the fluid motions may be turbulent.

Once a turbulent state is recognized, it is interesting to measure at least the number of modes involved in the

* Corresponding author. Tel.: +213 71 59 38 57; fax: +213 33 81 21 43.
E-mail address: samir.rahal@lycos.com (S. Rahal).

0017-9310/$ - see front matter © 2008 Elsevier Ltd. All rights reserved.
doi:10.1016/j.ijheatmasstransfer.2008.01.021

Nomenclature

Latin symbols

a_{ij}	reconstruction coefficients
c	speed of sound
C	averaged covariance matrix
$C(t)$	correlation function
D_{kl}	KL dimension
E	total energy of the system
f	frequency
g	gravity
k	wavenumber
Pr	Prandtl number
$R(p)$	percentage of the energy contained in the first (p) modes
Ra	Rayleigh number
R_{cru}	radius of the crucible
R_{cry}	radius of the crystal
Re	Reynolds number
v	velocity
Z	acoustic impedance

Greek symbols

α	thermal diffusivity
β	volumetric coefficient of thermal expansion
κ	thermal conductivity
λ_j	the energy of the mode j
ν	kinematic viscosity
ρ	density
Ω	angular velocity of the crystal
Φ's	the empirical eigenfunctions or coherent structures
ΔT	difference of temperature applied between the crucible and the crystal

Abbreviations

Cz	Czochralski
KL	Karhunen–Loève
UVP	ultrasonic velocity profile

turbulent dynamics. For that purpose, the number of positive Lyapunov exponents is useful [9]. However, in an experiment, the calculation of these exponents becomes difficult to carry out when the number of positive exponents is larger than five [10]. Consequently, other methods have been tested, such as the proper orthogonal decomposition (Karhunen–Loève (KL) decomposition) [11,12] that has been applied to experimental [13–18] and numerical data sets [16,19–23]. More recently, it has been used to analyse the flow structures in a ventilated room [24] and has been applied to data sets of internal combustion engine flows [25]. This method is useful not only in estimating the number of the degrees of freedom of a dynamical system [16], but allows also theoretical models of the systems under study to be established [14,26]. The KL method converges rapidly even on data sets for which calculations of the Lyapunov exponents give wrong results because of insufficient data. The fact that it has only been few applications to experimental data sets is mainly due to a lack of a suitable measurement method that can provide data with sufficient spatial and time resolutions. Now, we can use the ultrasonic velocity profile (UVP) technique [27] which allows obtaining a suitable spatio-temporal velocity field.

As far as we know, no experimental work has been carried out to study the Cz flow, using tools such as the UVP velocity profiles, 2D Fourier spectra and a correlation function to recognize the flow regimes, the binary representation to study the scenario of transition to turbulence and the orthogonal decomposition method to estimate the number of degrees of freedom (number of involved modes, dimension) of the turbulent regimes. As it will be shown below, the use of such analysis methods allows a quantitative study of the Cz flow, which allows us recognizing the various flow regimes, the scenario of transition to turbulence and the number of modes involved for various experimental conditions. The obtained results might be useful in giving us the means to suppress or control the flow oscillations which need to be avoided in order to get free defect crystals. Simple theoretical models can also be established thanks to the KL method that allows calculating the number of degrees of freedom of the system (number of equations sufficient to study the system).

Using velocity fields obtained by the UVP technique and the analysis methods mentioned above, this paper allows showing the benefit and the feasibility of these methods and it is not meant to carry out a systematic parametric study. Indeed, the aim of this work is to show that the proposed techniques and methods, which were used in other applications, are efficient and may be used to carry out a comprehensive and systematic study of the real Cz growth system.

The paper is organized as follows: In Section 2, the experimental set-up and the UVP technique are briefly described; the analysis methods are described in Section 3. Some typical results are presented and discussed in Section 4 and conclusions are given in Section 5.

2. Experimental set-up and procedures

The experimental set-up, shown in Fig. 1, consisted of a simulated crucible (1) made of Pyrex glass (thermal conductivity $\kappa = 1.005$ W/mK at 25 °C and acoustic impedance $Z = 13.1 \times 10^6$ kg/sm^2) of 10-cm inner diameter and 10-cm height and a simulated crystal (2) of 3-cm diameter made of brass ($\kappa = 109$ W/mK at 25 °C). The crucible (1) was filled with 2 cSt silicone oil ($\kappa = 0.15$ W/mK at 25 °C, $Z = 0.74\times 10^6$ kg/sm^2, Prandtl number, $Pr = 28$ at $T = 25$ °C) as a model liquid (3). The simulated crystal

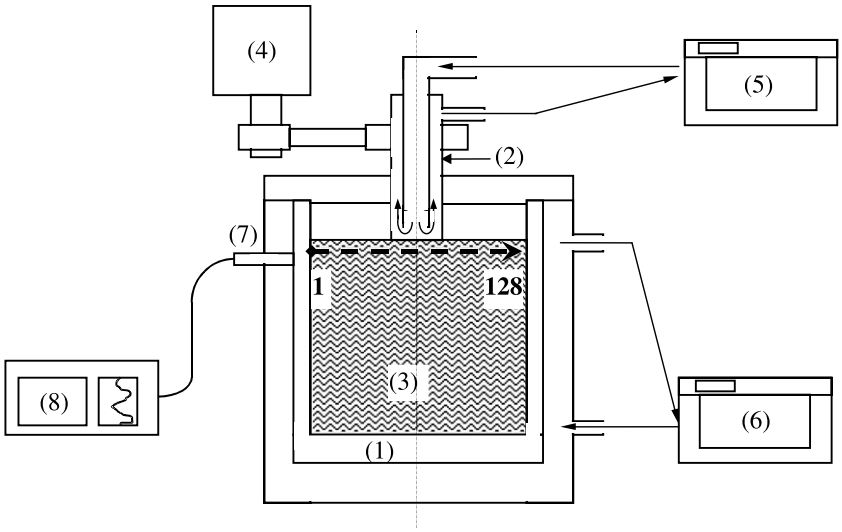

Fig. 1. Schematic of the experimental set-up, (1) simulated crucible, (2) simulated crystal, (3) silicone oil, (4) Motor to rotate the simulated crystal, (5) and (6) temperature-regulated baths, (7) UVP sensor, (8) UVP monitor. The measured velocity corresponds to the component of the flow velocity vector along the ultrasonic beam line which is drawn in a dashed line. The 128 positions at which velocities are measured are also shown.

(2) was rotated by a motor (4). The temperature difference between the crucible and the crystal was obtained by circulating cold and hot water flows, respectively, coming from two temperature-regulated baths (5, 6). The temperature fluctuations in both the crucible and the simulated crystal are about ±0.1 °C.

The UVP sensor (7) was set 1 cm below the liquid upper surface, and in contact with the outer wall of the crucible (Fig. 1). The measured velocity corresponds to the component of the flow velocity vector along the ultrasonic beam line [28], which is shown in Fig. 1, in a dashed line. The 128 positions at which velocities are measured are also shown. The measuring volume of each data point has a disc shape of radius 2 mm and thickness 0.75 mm. The UVP apparatus used in this work is the Met-Flow model X-1. The ultrasound transducer (7) was operated with a basic frequency of 4 MHz and a beam diameter of 4 mm. The other parameters of the measurements are given in Table 1. From the value of the speed of sound in the silicone oil (Table 2) and for $f = 4$ MHz, a wavelength of the ultrasound of 0.25 mm can be deduced. The divergence of the ultrasonic beam generated by the transducer used in our experiments being low (±4°), the diameter of the beam could then reach a maximum value of 15 mm. Actually, this value is thought to be less because of the focusing effect of the cylindrical wall [29].

Table 1
Parameters of the UVP measurements

Parameter	Value
Basic frequency of ultrasound	4 MHz
Ultrasonic beam diameter	4 mm
Number of measurement points (channels)	128
Number of profiles	1024
Spatial resolution	0.74 mm
Velocity resolution	0.48 mm/s
PRF	976 Hz
Divergence of the ultrasound beam	±4 °
Maximum velocity	61 mm/s

Table 2
Properties of the 2 cSt silicone oil at 25 °C

Property	Value
Density (ρ)	0.873×10^3 (kg/m^3)
Kinematic viscosity (ν)	2.0×10^6 (m^2/s)
Volumetric coefficient (β)	0.24×10^{-3} (K^{-1})
Thermal diffusivity (α)	7.1×10^{-8} (m^2/s)
Sound velocity (c)	1000 m/s
Acoustic impedance (Z)	0.74×10^6 kg/sm^2
Thermal conductivity (κ)	0.15 W/mK

The flow was visualized (Fig. 2) in the vertical median plane using a light sheet and powdered ferrite as tracer. As only ferrite particles with a density close to that of the silicone oil ($\rho = 0.873$ g/cm^3) are used (lighter and heavier particles being excluded before to start the experiments), the particles stay in suspension and follow the flow motions. It can also be noticed that the deflections of the ultrasound beam due to the interaction of the waves with the ferrite particles is less than 1° in our experimental conditions and can be considered as negligible [29].

The dimensions of our configuration are close to those used in [6] by Liu and Kakimoto, who studied a system with a crystal of 3-cm diameter and a crucible of 6.4-cm diameter. In the commercial scale Czochralski growth system of [8], a crystal of 15-cm diameter and a crucible of 46-cm diameter were used. The ratio of the crucible's diameter to that of the crystal is close to 3 in both our simulated configuration and in the commercial scale Czochralski system [8]. The flow behaviour in our configuration is then expected to reflect that of the commercial scale system. As for the fluid, the 2 cSt silicone oil has been chosen, because it has a small Prandtl number ($Pr = 28$) and since

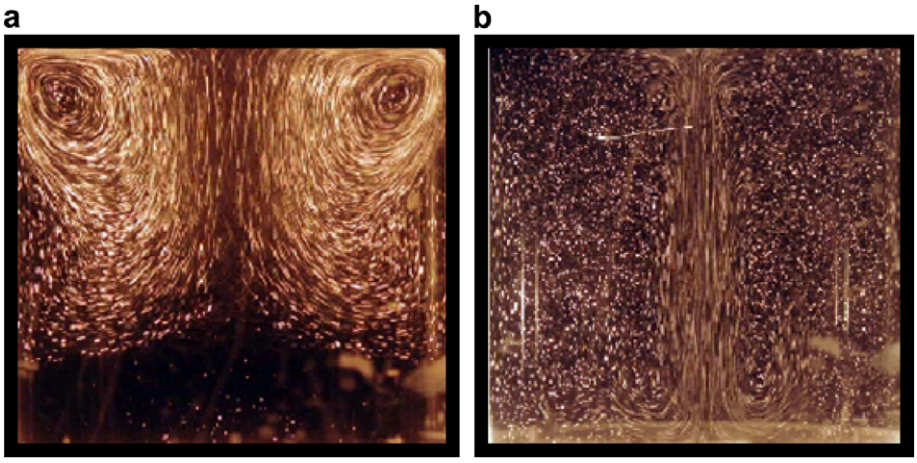

Fig. 2. Observed patterns, in the crucible's vertical median plane, taken with 1 s exposure time, in 2 cSt silicone oil. (a) $Ra = 0$, $Re = 5.9 \times 10^2$. (b) $Ra = 10^7$, $Re = 0$.

it is transparent, the flow visualization could be carried out. In the real Cz system, it is not possible to visualize the flow patterns using optical techniques because the melt is opaque and it is also difficult to measure temperature or velocity fields because of the high temperature and reactivity of the melt. Therefore, simulation with a model liquid, as in our study, is usually adopted in order to comprehend the general aspects of the flow behaviour.

The UVP technique [27] has been chosen because it allows getting a sufficient number of simultaneous measurements which cannot be obtained using the other classical measurement techniques which are limited by the number of sensors and/or data acquisition channels. Indeed the UVP allows overcoming efficiently this problem. This method uses the pulsed echography of an ultrasound. An ultrasound pulse is emitted from a transducer along the measurement line (corresponding to the diameter of the crucible in our experiment), and the same transducer receives the echo reflected back from particles scattered in the fluid.

The position information is given by the time elapsing between the pulse emission and the echo reception, and velocity information is obtained from the Doppler shift in the frequency at each instant. As the temperature was carefully controlled by a thermocouple in the vicinity of the measurement line, the input sound velocity parameter was corrected according to the actual value of the temperature. Instantaneous temperature fluctuations of about ± 0.3 K were detected inside the flow. If the temperature dependence of the speed of sound is taken into account, the maximum uncertainty in the determination of the measuring depth (i.e. the position information) is about 0.1 mm which is less than the spatial resolution, which is equal to 0.74 mm (Table 1).

As the Doppler shift method relies upon echoes from particles scattered in the silicon oil, optimal particles should have a density close to that of the liquid, in order to stay in suspension and follow the motions of the fluid as mentioned above. As for the particle size, if it is larger than the ultrasound wavelength, the waves are reflected and refracted by the particles. In such case, the direction of the propagation and the intensity of the wave are modified. On the other hand, if the size of a particle is smaller than the wavelength, another effect will occur, that is named scattering, for which, a small amount of the ultrasonic energy is reflected in all directions. As for the intensity and the direction of propagation of the waves, they are not practically affected by the scattering effect. Therefore particles smaller than the wavelength of the ultrasound are needed to carry out UVP measurements. The ferrite particles used in our experiments are about 40 μm in diameter, smaller then the ultrasound wavelength which has been calculated above (=0.25 mm).

Another crucial point of the UVP application is the transmission of the ultrasonic beam through the lateral wall which depends on the ratio of the acoustic impedances of both the lateral wall and the silicone oil. The acoustic impedance being given by $Z = \rho \times c$ (c is the speed of sound and ρ the density). The acoustic impedance of the Pyrex glass is $Z = 13.1 \times 10^6$ kg/sm^2 and that of the silicon oil $Z = 0.74 \times 10^6$ kg/sm^2. These acoustic impedances can be considered as sufficiently not far to allow the transmission of an ultrasound wave with sufficient energy and amplitude at the wall–liquid interface.

Fig. 3 shows examples of velocity fields obtained using the UVP technique described above. There are 128 measurement points per profile and one experimental run consists of 1024 temporal profiles that are successively collected. The speed and direction of the flow are colour-coded. Velocities of the particles moving towards the UVP sensor are represented in green to blue and those of particles moving away from the UVP sensor indicated in red to yellow. The measured velocity fields were used as the basis on which the analysis has been conducted.

The pulse repetition frequency (PRF) of the ultrasonic wave is an essential parameter in the UVP measurements since the time, t_{PRF}, between two ultrasound emissions

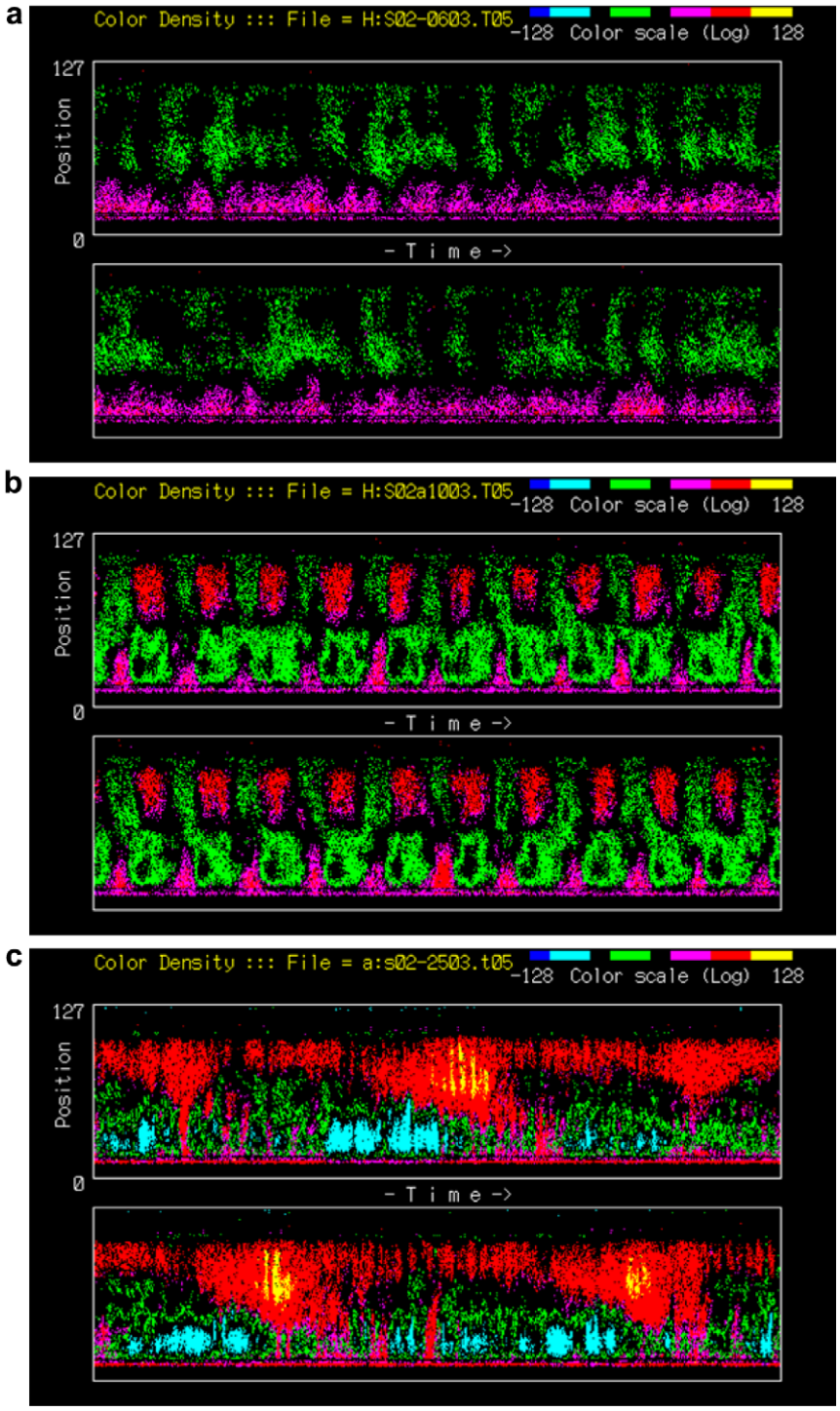

Fig. 3. Velocity profiles for a fixed Ra ($=10^7$). (a) Steady state ($Re = 7.1 \times 10^2$). (b) Quasi-periodic state ($Re = 1.2 \times 10^3$). (c) Turbulent state ($Re = 2.9 \times 10^3$). Velocities of the particles moving towards the UVP sensor are represented in green to blue and those of particles moving away from the UVP sensor indicated in red to yellow. There are 128 measurement points per profile and 1024 temporal profiles. (For interpretation of the references to colour in this figure legend, the reader is referred to the web version of this article.)

determines both the length and the velocity resolution. Indeed, if the time between two wave emissions is too long, fast particles could move too fast to yield echoes that can be detected. On the other hand, too slow particles do not allow showing detectable displacements between two emissions if the PRF is too large. The PRF parameter has then to be carefully chosen. For our experiments, PRF was taken equal to 976 Hz and the corresponding time, $t_{PRF} \approx 1$ ms, can be considered as very sufficient to capture transient flow behaviour.

The maximum depth (D_{max}) and velocity (V_{max}) along the beam that can be measured being linked by $D_{max} \times$

$V_{max} = c^2/8f_e$, where c is the speed of sound in the silicone oil and f_e the emission frequency (=4 MHz in our case) [29]. As for our experiments, $D_{max} = 512$ mm, the maximum velocity that can be measured is $V_{max} = 61$ mm/s and the velocity resolution is equal to 0.48 mm/s (Table 1).

The flow was studied as a function of the relevant physical parameters in the Czochralski flow, namely, the Rayleigh number, $Ra = g\beta\Delta T R_{cru}^3/v\alpha$ (from 0 to 7.2×10^7) and the Reynolds number, $Re = \Omega R_{cry}^2/v$ (from 0 to 3.9×10^3), where R_{cry} and R_{cru} are the radii of the crystal and the crucible respectively; ΔT is the temperature difference applied between the crucible and the crystal; β is the volumetric coefficient of thermal expansion, v is the kinematic viscosity, α is the thermal diffusivity, Ω is the angular velocity of the crystal rotation, and g the gravity acceleration. The physical properties of the 2 cst silicone oil are given in Table 2.

If a mixed convection parameter, $A = Ra/Pr \cdot Re^2$, is defined, as in [30], the flow resulting from the application of both the rotation and buoyancy effects can be classified, as a function of (A), as below:

(i) If $0 \leqslant A < 0.5$: the forced convection (rotation effects) is dominant,
(ii) if $A \approx 0.5$: the rotation and buoyancy effects are of equal force,
(iii) and the buoyancy effects are dominant when $A > 0.5$.

3. Analysis methods

The spatio-temporal nature of the flow is clearly obtained and displayed on the UVP data (Fig. 3). However, to further understand the phenomena involved and to reach corroborating conclusions from results obtained by various means, we used the following methods.

3.1. Fourier spectrum

The UVP data can be analyzed by a 2D Fourier transform to generate 2D spectra. The evolution of the flow through its velocity fields can then be studied using the corresponding frequency-wavenumber spectra, the same way as in [31]. This method is very useful because it allows to gather on the same figure the temporal modes (through the frequency of oscillation, f, axis corresponding to the time axis in the velocity profile) and spatial modes (through the wavenumber, k, axis corresponding to the position axis in the velocity profile) (Fig. 4).

3.2. Correlation function

We can also compute the temporal correlation function, defined as:

$$C(t) = \frac{\langle [v(x,t) - \langle v \rangle][v(x,o) - \langle v \rangle] \rangle}{\langle v^2 \rangle} \quad (1)$$

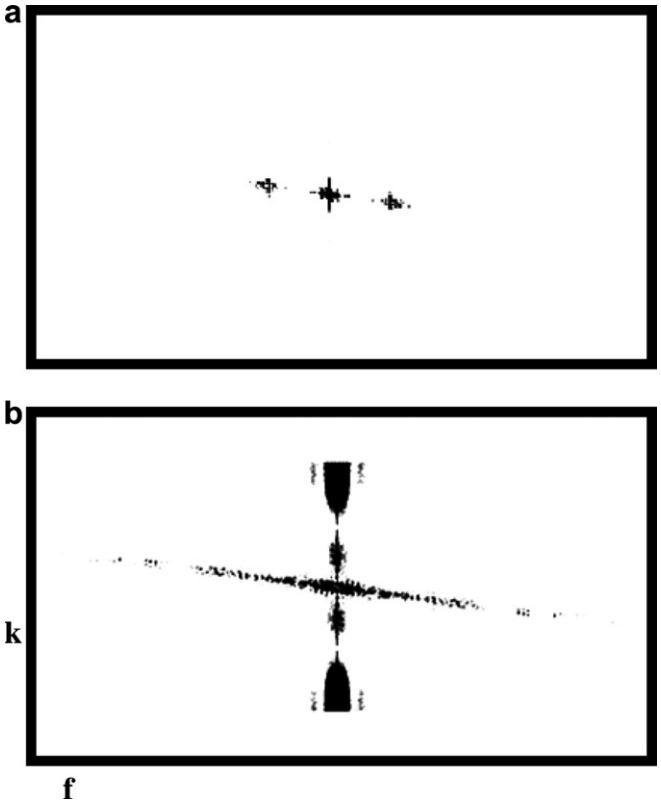

Fig. 4. 2D power spectra of the velocity profiles of Fig. 3b and c. Horizontal and vertical axes are the frequency (f) and wavenumber (k) axes, respectively. $Ra = 10^7$. (a) Quasi-periodic state ($Re = 1.2 \times 10^3$). (b) Turbulent state ($Re = 2.9 \times 10^3$).

where $v(x, t)$ and $v(x, o)$ are the values of the velocity at different times and $\langle \quad \rangle$ denotes an average.

3.3. Binary representation

In order to know which scenario leads the Cz flow to the turbulent regime, the binary representation has been used, as in [10,32,33]. Indeed, in [10,32,33], the simultaneous coexistence of two kinds (laminar and turbulent) of qualitatively different domains was an indicator to search for a criterion which distinguishes their different spatial and temporal characteristics and thereby enabling to recognize the scenario of transition to turbulence. In laminar domains (LD), the time evolution, at a given point, is either steady or oscillating in time leading to a local mono-periodic or quasi-periodic regime. On the other hand, turbulent domains (TD) are regions without spatial coherence and the time evolution is chaotic. The UVP velocity field can then be reduced to a binary representation (laminar, turbulent) which allows us to perform statistics on LD and TD in the same way as in [10,32,33]. In our study, a temporal criterion has been used, the velocity differences between successive acquisitions were computed and compared to a cut-off value (δ). A point in the binary representation, corresponding to a velocity variation, is considered as laminar if $v(x, t + \Delta t) - v(x, t) \leqslant \delta$, otherwise it is turbulent. We ver-

ified that, all the values of (δ) within the range (1.5–2) lead to the same binary representation. Calculations were carried out with $\delta = 1.75$.

3.4. The proper orthogonal decomposition (Karhunen–Loève (KL) decomposition)

The proper orthogonal decomposition (POD) is a method for extracting an orthogonal basis (POD basis) for the decomposition of a given collection of data which is generally a set of spatio-temporal signals. POD has its roots in statistical analysis and has appeared with various names, including: principal component analysis, empirical eigenfunctions, Karhunen–Loève decomposition, and empirical orthogonal eigenfunctions. The POD has been extensively used in numerous applications and was first introduced in turbulence by Lumley [34]. The benefit of using POD is the utilization of its fast convergence to get well resolved simulations with a lower number of modes than a simulation using, for example, Fourier decompositions.

As the KL decomposition applied to dynamic systems has been described in detail in many publications [11,12], we will restrict ourselves here to describing the overall concept.

Choosing the appropriate input collection is a vital part of the POD method since the POD basis only reflects information provided by the input collection. An input collection of time snapshots is then frequently chosen when the POD basis is used for model reduction. In our study, the field to be decomposed using the KL method is a velocity field v (x, t) obtained by UVP. Each data set is composed of 128×1024 velocities in a matrix form.

Let us consider a data set

$$\{v_i, i = 1, \ldots\ldots, n\} \tag{2}$$

where each v_i is a m-vector

$$v_i = (v_{1i}, \ldots, v_{mi})^T \tag{3}$$

where $n = 1024$ and $m = 128$ in this case.

The principle of the method is to find a set of vectors that forms a basis. Thus the resolution leads to an eigenvalue problem for the Φ's:

$$C\Phi_j = \lambda_j \Phi_j \tag{4}$$

where,

$$C = \langle v_i v_i^{\mathrm{T}} \rangle \tag{5}$$

is the ensemble averaged covariance matrix, and Φ's are called the eigenfunctions or coherent structures. C is a $m \times m$ (128×128) symmetrical non-negative matrix, and consequently determines a complete set of orthogonal eigenvectors, and real non-negative eigenvalues. The relative magnitude of each eigenvalue with respect to all the others gives a measure of the importance of the corresponding eigenfunction in representing elements of the input collection. POD inherently orders the basis elements by their relative importance. The eigenvalues are then ordered, as:

$$\lambda_1 \geqslant \lambda_2 \geqslant \lambda_3 \ldots\ldots \geqslant \lambda_m \tag{6}$$

where λ_j is the energy of mode j and

$$E = \sum_{j=1}^{m} \lambda_j \tag{7}$$

the total energy of the system.

Once, the Φ's are determined by finding the eigenvectors of C, the a_{ij} coefficients can be found by projecting the data vectors onto each eigenvector in turn:

$$a_{ij} = (v_i, \Phi_j) \tag{8}$$

These coefficients (a_{ij}) are referred to as "reconstruction coefficients".

Two widely used methods for determining the optimal dimension of the reduced-order system are: (i) computing the percentage of energy extracted; (ii) plotting the POD eigenvalues. Each eigenvalue represents the energy contributed by each mode. Thus by including more POD modes, one increases the total percentage of energy captured by the reduced-order POD representation. As for us, we have defined the quantity:

$$R(p) = \sum_{j=1}^{p} \frac{\lambda_j}{E} \tag{9}$$

which is the percentage of the energy contained in the first (p) modes. In order to estimate the dimension of a flow, we used the KL dimension D_{kl}, which is the number of modes capturing 90 % of the total energy of the flow [18].

4. Results and discussion

In the Cz flow, the most important driving forces are (i) the centrifugal force due to the crystal rotation; and (ii) the buoyancy force due to the temperature gradient. The corresponding flows are shown in Fig. 2a and b, respectively. The first flow has the shape of a ring rotating around its own axis and the second is an axisymetric flow. As a result of the combination of the flows induced by these forces and other forces, such as the Marangoni convection, the flow behaves in a very complex manner in the crucible (Figs. 5 and 6).

For a given Rayleigh number ($Ra = 10^7$, $\Delta T = 5$ K), as the crystal rate of rotation increases (increase of Ω from 60 rpm to 250 rpm and the Reynolds number from 7.1×10^2 to 2.9×10^3), more vortices are involved and the flow becomes more complex (Fig. 5). As for the mixed convection parameter, (A), it varies from 0.708 which corresponds to dominant buoyancy effects for $Re = 7.1 \times 10^2$ to $A = 0.042$ corresponding to dominant rotation effects for $Re = 2.9 \times 10^3$. The influence of the temperature difference (Ra number) on the flow can be seen in Fig. 6. For a given Re (1.8×10^3, $\Omega = 150$ rpm), as the temperature

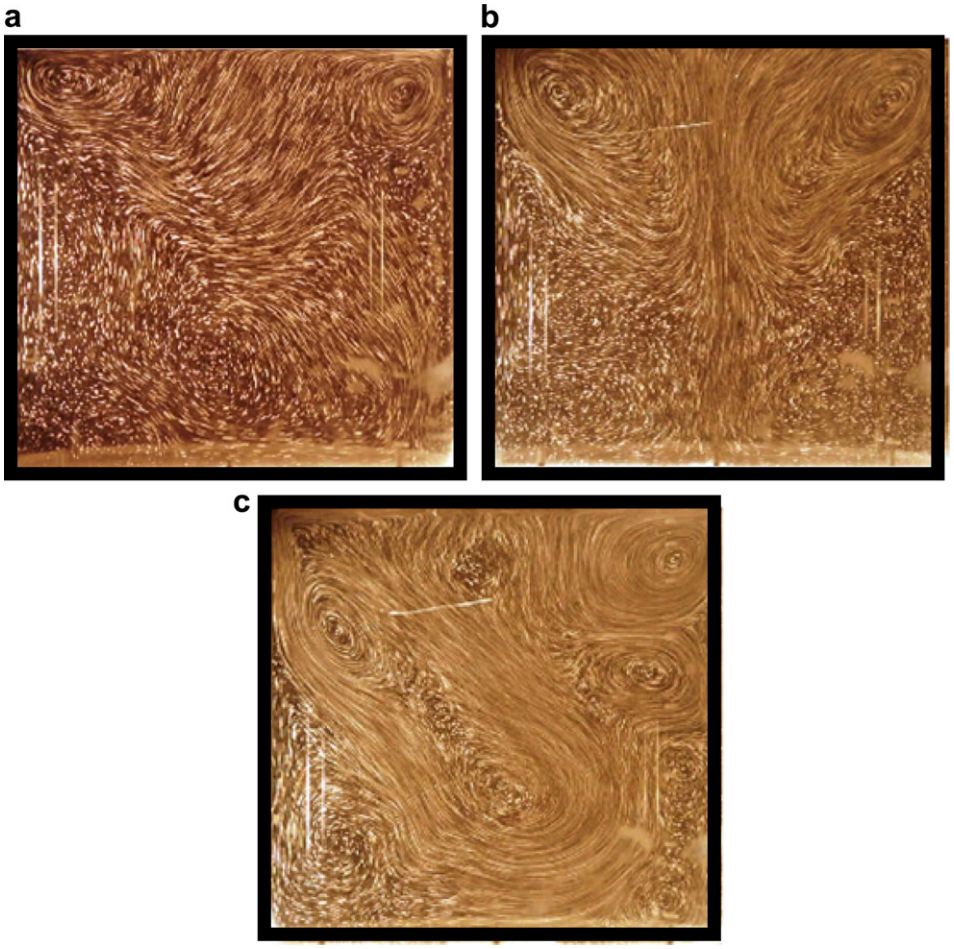

Fig. 5. Observed patterns, taken with 1 s exposure time, in 2 cSt silicone oil. $Ra = 10^7$. (a) $Re = 7.1 \times 10^2$. (b) $Re = 1.2 \times 10^3$. (c) $Re = 2.9 \times 10^3$.

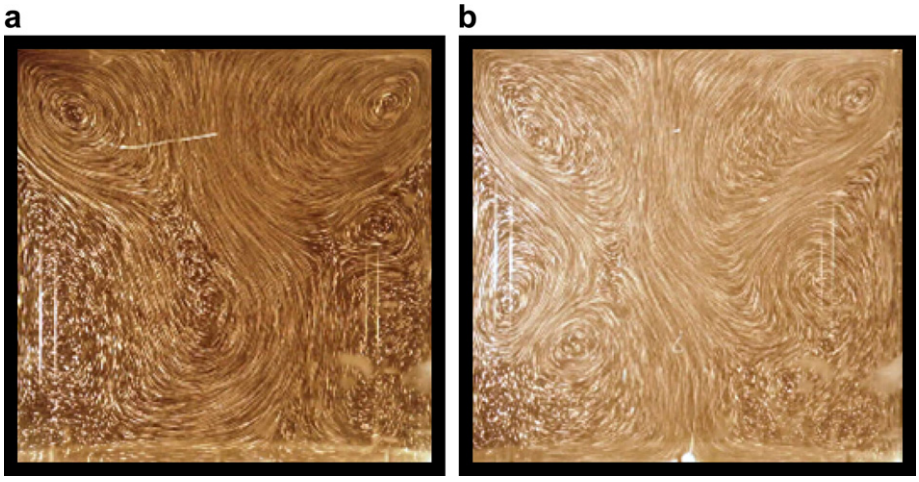

Fig. 6. Observed patterns, taken with 1 s exposure time, in 2 cSt silicone oil. $Re = 1.8 \times 10^3$. (a) $Ra = 10^7$. (b) $Ra = 2.1 \times 10^7$.

difference is increased (from $\Delta T = 5$ to 10 K and *Ra* number increasing from 10^7 to 2.1×10^7), more vortices are involved and the flow becomes more and more complex. (*A*) Varies from 0.11 for $Ra = 10^7$ to $A = 0.23$ for $Ra = 2.1 \times 10^7$ indicating that the rotation effects (forced convection) are dominant.

Fig. 5 shows qualitatively the increase of the flow complexity, as Re is increased, for a fixed value of the *Ra* number. Velocity profiles corresponding to the flows of Fig. 5 are shown in Fig. 3. Fig. 3a corresponds to a steady state without any temporal variation of the velocity, Fig. 3b corresponds to an oscillatory quasi-periodic state

velocity and Fig. 3c corresponds to a turbulent state without periodicity in either space or in time.

The application of 2D Fourier transforms to the velocity fields of Fig. 3b and c, the same way as in [31], allows getting the spectra shown in Fig. 4. Indeed, Fig. 4a shows a spectrum corresponding to an oscillatory quasi-periodic state with frequencies equal, respectively, to 0.038, 0.04 and 0.042 Hz, whereas the spectrum of Fig. 4b corresponds to a turbulent state with large dispersions both in the frequency of oscillation (f) (from 0.007 to 0.08 Hz) and the wavenumber (k) (from 1.52 to 3.82), indicating the presence of a large number of temporal and spatial modes, which is the characteristic of a turbulent flow. It can also be noticed that the spatial modes, corresponding to $k = 2.67 \pm 0.26$ and located at the middle of the spectrum, are coupled to the temporal modes. So, the evolution of these Fourier spectra as a function of Re for a fixed Ra ($=10^7$) clearly shows the difference between the various states and may allow to locate accurately the transition to turbulence.

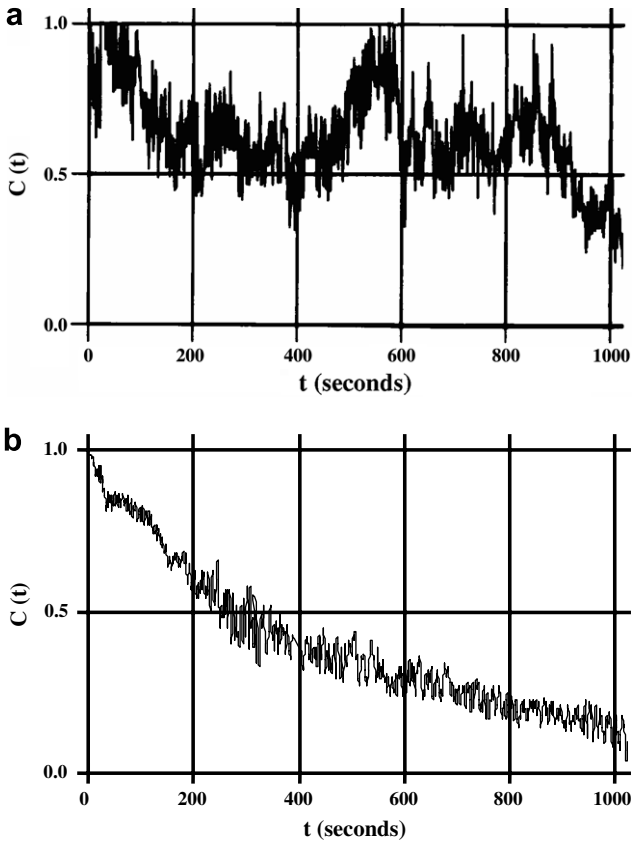

Fig. 7. Temporal correlation functions for the velocity fields corresponding to: (a): $Re = 2.9 \times 10^3$, (b): $Re = 3.4 \times 10^3$. $Ra = 10^7$.

The correlation function shown in Fig. 7a and corresponding to the velocity field at $Re = 2.9 \times 10^3$ and $Ra = 10^7$ appears noisy and does not strictly decrease to zero. When the Reynolds number is further increased to $Re = 3.4 \times 10^3$, the corresponding correlation function (Fig. 7b) does decrease monotonically to zero, that is, indicating a loss of correlation of the system which is a characteristic of a turbulent state. Thus, the zone of transition to turbulence, is between $Re = 1.2 \times 10^3$ and $Re = 3.4 \times 10^3$. This transition to turbulence has been characterized using independent analysis methods, namely the 2D spectra and the correlation function.

Experiments conducted by other authors have shown two kinds of fluctuations [35,36], chaotic when only the free convection is present (with only the temperature gradient); and periodic variation when rotation is involved. Indeed, the temperature gradient between the crucible and the crystal affects significantly the flow in the crucible, particularly in the close vicinity of the crystal growth interface [37]. More recently, an intermittent transition to chaotic flow has also been observed in a Cz system, for which chaotic temperature fluctuations have been detected near the crystal–melt interface [38].

Using the binary representation method described above, the spatio-temporal diagrams are shown in Fig. 8

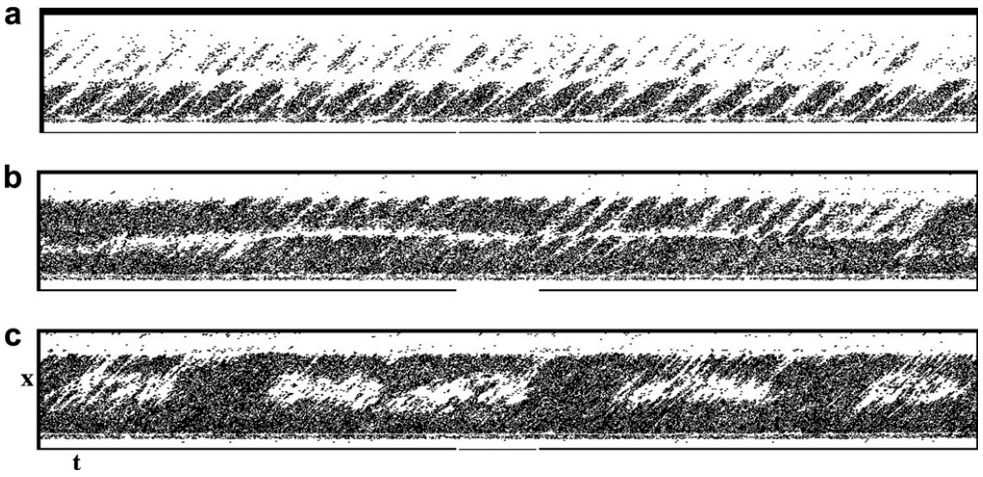

Fig. 8. Binary representations of the velocity profiles for various values of Re ((a): 1.2 10^3, (b): 1.8 $\times 10^3$ and (c): 2.9×10^3). The dark and white areas correspond to turbulent and laminar domains respectively, as defined by the criterion in the text.

for different values of Re at a given Ra. When Re was increased from 1.2×10^3 to 2.9×10^3, turbulent areas propagate and connect within the laminar domains that become fewer as in [10,32,33] where the transition to turbulence via spatio-temporal intermittency was observed for Rayleigh-Bénard convection. In order to characterize the global degree of turbulence, the mean turbulent fraction (F_t) and laminar fraction (F_l) have been computed, as in [10,32,33], where (F_t) refers to the averaged total area occupied by the turbulent patches divided by the total extent of the field, $F_l = 1 - F_t \cdot (F_t)$ and (F_l) are plotted as functions of Re in Fig. 9. It can be noticed that (F_t) increases and (F_l) decreases as Re is increased, as in [10,32,33] and for $Re \geqslant 2.9 \times 10^3$, ($F_t$) is larger than ($F_l$).

Once a turbulent flow is recognized, it is interesting to estimate the number of modes that may produce such behaviour. For that purpose, the POD method has been applied. The cumulative energy $R(p)$ versus (p) is shown in Fig. 10 for different values of Re at a given Ra ($=10^7$). Clearly, $R(p)$ reaches 90% of the total energy, at lower (p) values, for highest Re, whereas for a given value of Re ($=1.8 \times 10^3$), the opposite was observed: 90% of the total energy is reached for lowest values of Ra (Fig. 11). In Fig. 12, the dimension D_{kl} is plotted as a function of Ra for various values of the Re number. It can be noticed that, at a given Ra, D_{kl} decreases as Re is increased, and increases with Ra for a given Re. Thus, it can be concluded that the rotation effects are stabilizing the flow, and the temperature gradients have a destabilizing role. Indeed, the increase of the Re number (rotation effects) induces the decrease of the system dimension (fewer modes are involved in the dynamics). Conversely, more modes and oscillations are involved when the buoyancy effects (Ra number) are increased.

An example of the reconstruction coefficients, a_{i1} ($i = 0$, 1023 and $j = 1$), for $Re = 1.2 \times 10^3$ and $Ra = 10^7$, plotted as a function of i (time), is shown in Fig. 13. The reconstruction coefficients show a periodicity, which is associated with a quasi-periodic oscillatory flow, in a good agreement with the field showed in Fig. 3b and the spectrum of Fig. 4a. On the other hand, in Fig. 14, the reconstruction coefficients a_{1j} ($i = 1$, $j = 0$, 127) for $Re =$

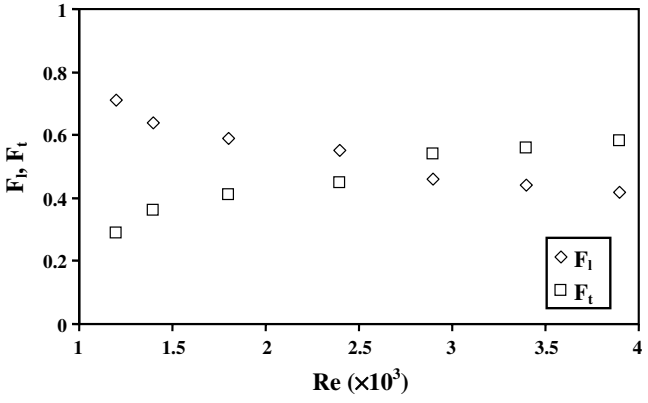

Fig. 9. Mean turbulent fraction F_t and laminar fraction F_l as functions of Re. $Ra = 10^7$ ($\Delta T = 5$ K).

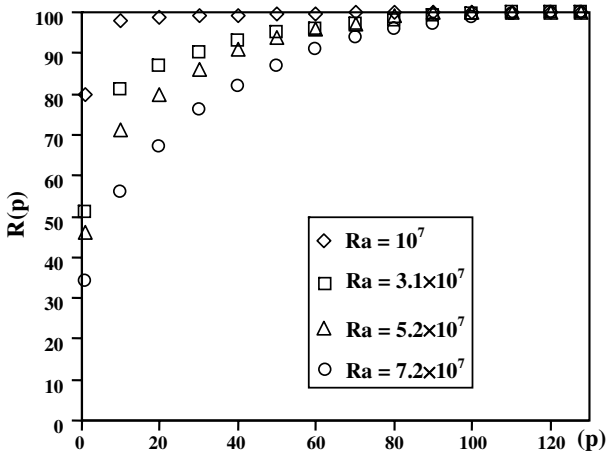

Fig. 11. The cumulative energy $R(p)$ versus (p) for various Ra. $Re = 1.8 \times 10^3$ ($\Omega = 150$ rpm).

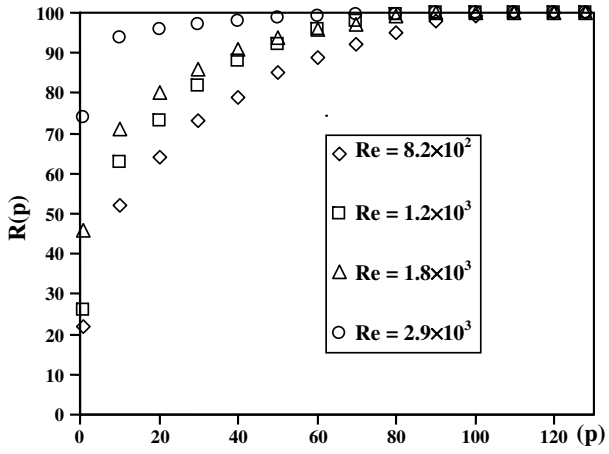

Fig. 10. The cumulative energy $R(p)$ versus (p) for various Re. $Ra = 10^7$ ($\Delta T = 5$ K).

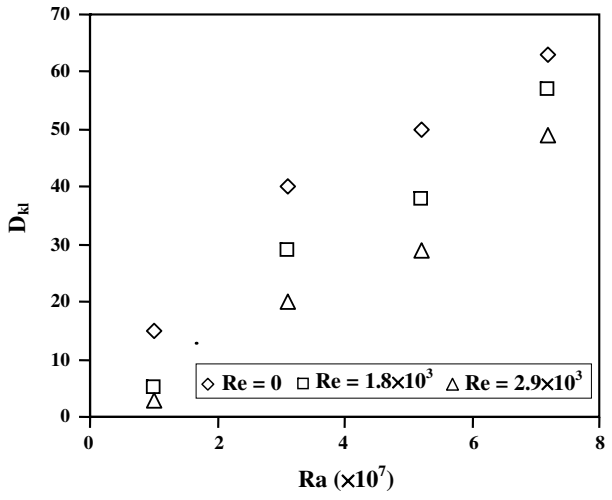

Fig. 12. The dimension D_{kl} as a function of Ra for various Re.

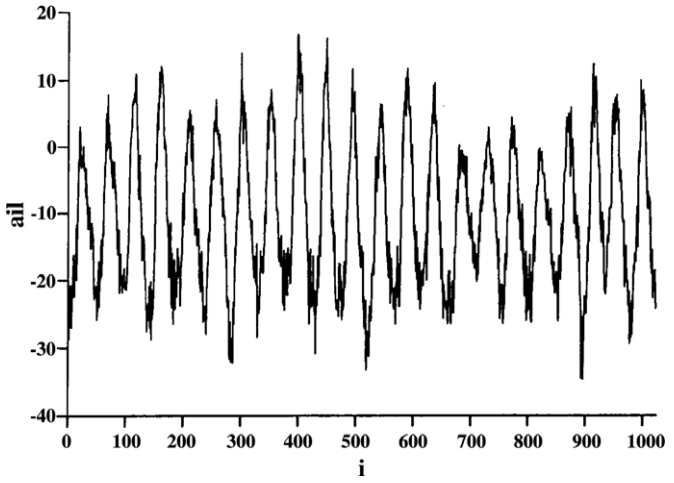

Fig. 13. Reconstruction coefficients a_{i1} versus i. $Re = 1.2 \times 10^3$, $Ra = 10^7$.

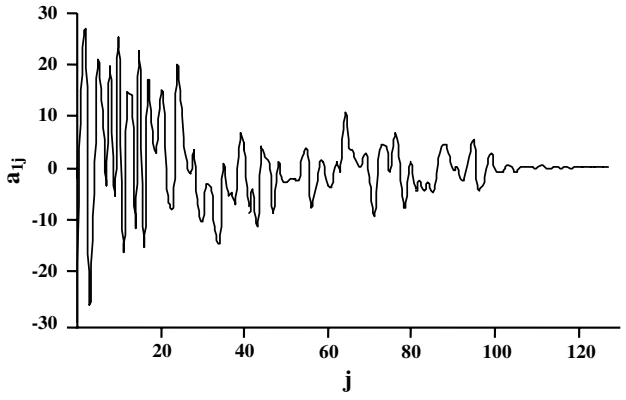

Fig. 14. Reconstruction coefficients a_{1j} versus j. $Re = 1.2 \times 10^3$, $Ra = 10^7$.

1.2×10^3 and $Ra = 10^7$, are plotted as a function of j (position). As it can be seen, there is no spatial periodicity, in agreement with the measured velocity field of Fig. 3b and the spectrum of Fig. 4a. Figs. 13 and 14, shown above, allow concluding that the reconstruction coefficients, obtained using the KL method, reflect accurately the actual flow and then can be used to build simple theoretical models of the system.

5. Conclusions

In this paper devoted to a simulated Czochralski system, steady, quasi-periodic and turbulent flows, were successively observed, as the Reynolds number was increased, for a fixed Rayleigh number. The various regimes were recognized using the velocity fields, their 2D Fourier spectra and a correlation function.

By reducing the space–time dynamics of the velocity fields to a binary representation, the transition to turbulence was found to occur via spatio-temporal intermittency, the most known route to turbulence in such spatially extended systems [10,32,33].

The numbers of modes (dimensions), involved in the dynamics of turbulent flows, were estimated, using the KL decomposition. As far as we know, this method has been used for the first time to study the Cz convective flows, which provided us with information on the most important modes and thus may allow simple theoretical models to be established. The large rotation rates of the crystal were found to stabilize the flow, and conversely the temperature gradients destabilize the flow. Indeed, the increase of the rotation effects reduces the number of involved modes and oscillations, and conversely, as expected, the increase of the buoyancy effects induces more modes to be involved in the dynamics. Thus, the flow oscillations can be reduced either by increasing the crystal rotation rate to the adequate value, as shown in this study and in [30], or by imposing a magnetic field [5]. The reconstruction coefficients obtained using the KL method were found to reflect the actual flow and then can be used to built simple theoretical models of the system.

To summarize, the various analysis methods used in this paper allowed reaching complementary results and corroborating conclusions. These methods will therefore allow a complete characterization of the convective regimes in the real Cz growth system.

References

[1] V. Prasad, H. Zhang, A.P. Anselmo, Transport phenomena in Czochralski growth process, in: J.P. Hartnett, T.F. Irvine Jr., Y.I. Cho, G.A. Greene (Eds.), Advances in Heat Transfer, vol. 30, Academic Press, 1997, pp. 313–435.

[2] W. Miller, U. Rehse, K. Bottcher, Melt convection in a Czochralski crucible, Cryst. Res. Technol. 34 (4) (1999) 481–489.

[3] V.V. Kalaev, A.I. Zhmakin, E.M. Smirnov, Modelling of turbulent melt convection during Czochralski bulk crystal growth, J. Turbulence 3 (2002) 13–24.

[4] A. Voigt, C. Weichmann, J. Nitschkowski, E. Dormberger, R. Holz, Transient and quasi-stationary simulation of heat and mass transfer in Czochralski silicon crystal growth, Cryst. Res. Technol. 38 (6) (2003) 499–505.

[5] Y.R. Li, D.F. Ruan, N. Imaishi, S.Y. Wu, L. Peng, D.L. Zeng, Global simulation of a silicon Czochralski furnace in an axial magnetic field, Int. J. Heat Mass Transfer 46 (15) (2003) 2887–2898.

[6] L. Liu, K. Kakimoto, Partly three-dimensional global modelling of a silicon Cz furnace. I. Principles, formulation and implementation of the model, Int. J. Heat Mass Transfer 48 (22) (2005) 4481–4491.

[7] A. Hirata, Y. Okano, K. Yakushiji, B. Harrison, Czochralski process, in: A.S. Mujumdar, R.A. Mashelkar (Eds.), Advances in Transport Processes, VIII, Elsevier, 1992.

[8] T. Kanda, M. Hourai, S. Miki, T. Shigematsu, H. Tomokage, T. Miyano, H. Morita, A. Shintani, Influence of melt-temperature fluctuations on striation formation in large-scale Czochralski Si growth systems, J. Cryst. Growth 166 (1996) 663–668.

[9] J.P. Eckmann, S. Oliffson-Kamphorst, D. Ruelle, S. Ciliberto, Liapunov exponents from time series, Phys. Rev. A 34 (1986) 4971–4979.

[10] M. Caponeri, S. Ciliberto, Thermodynamics aspects of the transition to spatiotemporal chaos, Physica D 58 (1992) 365–383.

[11] J.L. Lumley, Coherent structures in turbulence, in: R.E. Meyer (Ed.), Transition and Turbulence, Academic Press, New York, 1981, pp. 215–242.

[12] G. Berkooz, P. Holmes, J.L. Lumley, The proper orthogonal decomposition in the analysis of turbulent flow, Ann. Rev. Fluid Mech. 25 (1993) 539–575.

[13] D.S. Broomhead, G.P. King, Extracting qualitative dynamics from experimental data, Physica D 20 (1986) 217–236.
[14] N. Aubry, P. Holmes, J.L. Lumley, E. Stone, The dynamics of coherent structures in the wall region of a turbulent boundary layer, J. Fluid Mech. 192 (1988) 115–173.
[15] A. Glezer, Z. Kadioglu, A.J. Pearlstein, Development of an extended proper orthogonal decomposition and its application to a time periodically forced plane mixing layer, Phys. Fluids A 1 (8) (1989) 1363–1373.
[16] S. Ciliberto, B. Nicolaenko, Estimating the number of degrees of freedom in spatially extended systems, Europhys. Lett. 14 (4) (1991) 303–308.
[17] M.P. Chauve, P. LeGal, Complex bi-orthogonal decomposition of a chain of coupled wakes, Physica D 58 (1992) 407–413.
[18] L. Sirovich, Empirical eigenfunctions and low dimensional systems, New Perspectives in Turbulence, Springer-Verlag, 1991, pp. 139–163.
[19] L. Sirovich, Chaotic dynamics of coherent structures, Physica D 37 (1989) 126–145.
[20] B. Knight, L. Sirovich, Kolmogorov inertial range for inhomogeneous turbulent flows, Phys. Rev. Lett. 65 (1990) 1356–1359.
[21] P. Moin, R. Moser, Characteristic-eddy decomposition of turbulence in a channel, J. Fluid Mech. 200 (1989) 471–509.
[22] L. Sirovich, K.S. Ball, L.R. Keefe, Plane waves and structures in turbulent channel flow, Phys. Fluids A 2 (12) (1990) 2217–2226.
[23] G.A. Webber, R.A. Handler, L. Sirovich, The Karhunen–Loeve decomposition of minimal channel flow, Phys. Fluids 9 (4) (1997) 1054–1066.
[24] J. Pedersen, K. Meyer, POD analysis of flow structures in a scale model of a ventilated room, Exp. Fluids 33 (6) (2002) 940–949.
[25] M. Fogleman, J. Lumley, D. Rempfer, D. Haworth, Application of the proper orthogonal decomposition to datasets of internal combustion engine flows, J. Turbulence 5 (2004) 1–18.
[26] L. Sirovich, J.D. Rodriguez, Coherent structures and chaos: a model problem, Phys. Lett. A 120 (1987) 211–214.
[27] Y. Takeda, Development of an ultrasound velocity profile monitor, Nucl. Eng. Des. 126 (1991) 277–284.
[28] Y. Takeda, Velocity profile measurements by ultrasound Doppler shift method, Int. J. Heat Fluid flow 7 (1986) 313–318.
[29] D. Brito, H.C. Nataf, P. Cardin, J. Aubert, J.P. Masson, Ultrasonic Doppler velocimetry in liquid gallium, Exp. Fluids 31 (2001) 653–663.
[30] J. Choi, H.J. Sung, Suppression of temperature oscillation in Czochralski convection by superimposing rotating flows, Int. J. Heat Mass Transfer 40 (1997) 1667–1675.
[31] Y. Inoue, S. Yamashita, K. Kondo, The ultrasonic velocity profile measurement of flow structure in the near field of a square free jet, Exp. Fluids 32 (2002) 170–178.
[32] F. Daviaud, M. Bonetti, M. Dubois, Transition to turbulence via spatiotemporal intermittency in one-dimensional Rayleigh-Bénard convection, Phys. Rev. A 42 (1990) 3388–3399.
[33] T. Yanagita, K. Kaneko, Rayleigh-Bénard convection patterns, chaos, spatiotemporal chaos and turbulence, Physica D 82 (1995) 288–313.
[34] J.L. Lumley, The structure of inhomogeneous turbulence, in: A.M. Yaglom, V.I. Tatarski (Eds.), Atmospheric Turbulence and Wave Propagation, Nauka, Moscow, 1967, pp. 166–178.
[35] P. Peshev, V. Nikolov, K. Iliev, Simulation studies of the hydrodynamics in high-temperature solutions for crystal growth by the TSSG method, J. Cryst. Growth 65 (1983) 173–186.
[36] K. Kakimoto, M. Eguchi, H. Watanabe, T. Hibiya, Flow instability of molten silicon in the Czochralski configuration, J. Cryst. Growth 102 (1990) 16–20.
[37] J.P. Fontaine, A. Randriamampianina, P. Bontoux, Numerical simulation of flow structures and instabilities occurring in a liquid-encapsulated Czochralski process, Phys. Fluids A 3 (10) (1991) 2310–2331.
[38] D. Schwabe, R.R. Sumathi, An intermittent transition to chaotic flow by crystal rotation during Czochralski growth, J. Cryst. Growth 275 (2005) 15–19.